

# Bjorken Initial Energy Density and Viscous Longitudinal Hydrodynamic Evolution in Xe-Xe Collisions

S. Biswal<sup>1</sup>, M. A. Bhat<sup>2,\*</sup>, A. Nayak<sup>2,3</sup>, S. I. Sahoo<sup>1,4</sup>, D. Dutta<sup>1,4</sup>, D. K. Mishra<sup>1,4</sup>, and P. K. Sahu<sup>1,2†</sup>

<sup>1</sup>*Homi Bhabha National Institute, Anushakti Nagar, Mumbai 400094, India.*

<sup>2</sup>*Institute of Physics, Sachivalaya Marg, Sainik School P.O., Bhubaneswar 751005, India.*

<sup>3</sup>*Department of Physics, School of Applied Sciences, KIIT, Bhubaneswar 751024, India.*

<sup>4</sup>*Nuclear Physics Division, Bhabha Atomic Research Centre, Mumbai 400085, India.*

We present a systematic study of the Bjorken initial energy density in Xe-Xe collisions at  $\sqrt{s_{NN}} = 5.44$  TeV, estimated using charged-particle multiplicity data and a generalized transverse overlap geometry applicable beyond the most central collisions. The dependence of the extracted energy density is examined by adopting both a constant formation time and a centrality-dependent formation time derived from Pb-Pb collisions at  $\sqrt{s_{NN}} = 5.02$  TeV. Corresponding Bjorken energy density estimates for Pb-Pb collisions are also presented for comparison. Taking the Bjorken energy density and formation time as initial conditions, the subsequent longitudinal evolution of the quark-gluon plasma (QGP) formed in these collisions is studied. Both ideal and first-order viscous boost-invariant hydrodynamics are employed to assess the influence of dissipation. We observe that viscous effects slow the longitudinal expansion and lead to entropy production dominated by early-time dynamics. The lifetime of the QGP is observed to increase with centrality and is substantially enhanced by viscous effects. These effects are highly sensitive to the choice of formation time, particularly in peripheral collisions. A comparative analysis of Xe-Xe and Pb-Pb collisions demonstrates that the longitudinal evolution is primarily controlled by the initial energy density scale set by the Bjorken prescription. Consequently, when this scale is comparable, both systems exhibit nearly identical evolution patterns, while appreciable distinctions emerge in peripheral collisions due to system-size and geometric effects.

## I. INTRODUCTION

In the early universe shortly after the Big Bang, a new state of matter is believed to have existed called Quark-Gluon Plasma (QGP) [1–4]. The existence of QGP in heavy-ion collisions was first proposed in the 1970s [5], an attempt to understand the behavior of high energy collisions between atomic nuclei.

Experimental evidence for the creation of the QGP was provided by the Relativistic Heavy Ion Collider (RHIC) through heavy-ion collisions, such as Au-Au interactions, at a center-of-mass energy of  $\sqrt{s_{NN}} = 200$  GeV [6–8]. These collisions produced a perfect fluid which is made up of quarks and gluons having the ratio of shear viscosity to entropy density ( $\eta/s$ ) smaller than that of any other known liquid [9–12]. The Large Hadron Collider Experiment (LHC) later confirmed its existence in Pb-Pb collisions [13, 14]. In other collision systems such as pp, p-Pb at LHC [15–18] and <sup>3</sup>He-Au, d-Au at RHIC [19] similar properties also have been observed.

The most compelling theoretical evidence comes from lattice QCD, which predicts a phase transition at a critical temperature of approximately 154 MeV [20]. This corresponds to a critical energy density ( $\varepsilon$ ) of about 0.7–1.3 GeV/fm<sup>3</sup>, at zero net-baryon density [21]. Estimates derived from charged-particle pseudo-rapidity distributions and elliptic flow measurements in central Au-Au collisions at  $\sqrt{s_{NN}} = 200$  GeV at RHIC indicate that,

the energy densities ( $\varepsilon$ )  $\geq 3$  GeV/fm<sup>3</sup> are achieved as the system approaches approximate equilibrium [22]. These measurements are about 15–20 times higher than the normal nuclear matter density. It is therefore essential to determine the extent of the space-time region in which a heavy-ion collision exceeds the critical energy density, as well as the degree of equilibration attended within that region. Consequently, the evolution of the energy density during the early stages of the collisions, within the first few fm, are of particular importance.

The evolution of the QGP fluid can be better understood through transport coefficients such as viscosity and entropy, as they are closely related to the underlying quark-gluon strong interactions [23]. On focusing the temperature dependence of viscosities, the theoretical calculations on the shear ( $\eta$ ) and bulk ( $\zeta$ ) viscosity have been extensively explored [24, 25] at vanishing baryon density or equivalently zero baryon chemical potential. The final observables of heavy-ion collisions [26, 27] are significantly affected by the viscosities of the QGP; therefore, their values can be constrained with the help of experimental data. In earlier studies of viscous hydrodynamics,  $\frac{\eta}{s} = 0.08 \sim 0.2$  [28, 29] was typically assumed to be constant throughout the entire evolution. Recently, the constraints on the temperature dependence of the shear and bulk viscosities of the baryon-free QGP [30, 31] have been obtained using Bayesian statistical analysis with multi-stage models which integrate initial conditions, viscous hydrodynamics and hadronic transport. These studies consistently find an overall value of  $\frac{\eta}{s} \approx 0.16$  for the baryon-free QGP near pseudo-critical temperature  $T_{pc} \approx 160$  MeV [32, 33].

\* asifqadir1994@gmail.com

† pradip@iopb.res.in

Entropy is generated in a viscous evolution, leading to a difference between the initial and final state entropies. In Au-Au collisions, explicit numerical simulations indicate that, in fluid evolution with viscosity to entropy ratio  $\frac{\eta}{s} = 0.08, 0.12$  and  $0.16$ , the corresponding entropy production can be  $20\%$ ,  $30\%$ , and  $50\%$ , respectively higher than the initial entropy [34]. These simulations further indicate that the entropy production in viscous hydrodynamics occurs rapidly, with the majority generated within the first  $2 - 4$  fm of evolution [35].

The evolution of the system created in ultra-relativistic heavy-ion collisions is driven by pressure gradients, expands collectively and cools until hadronization. The geometric anisotropies in the initial state is turned by the gradient driven expansion into anisotropic flow in the final state and the variations in size in the initial state into radial flow [36–38]. The azimuthal momentum anisotropy is quantified by the anisotropic flow [39–42], while the radial boost of the system, which influences the average transverse momentum of particles in each event is characterized by radial flow [43, 44].

It is not straight-forward to directly estimate the initial pressure and energy density in the experiment. Therefore, hydrodynamical calculations, which are based on the assumptions of local thermal equilibrium provide indirect constraints on these quantities. In the hydrodynamic framework, a proper time of  $\tau_0 \sim 1$  fm after the collisions is used as input for the subsequent evolution of the system formed in the heavy-ion collisions. Therefore, hydrodynamical model requires the initial energy density and net-baryon density, which are commonly assumed to be boost-invariant over a broad range of space-time rapidity.

The reaction dynamics can be better understood by the fluid hydrodynamics. In a collision at non-zero impact parameter, the anisotropy of the low  $p_T$  particles produced is described by the elliptic flow. This suggests that a collective flow of the particles exist following a hydrodynamical pressure gradient which is due to the initial eccentricity in a collision [45–47]. The elliptic flow [48] is successfully described by most of the hydrodynamical simulations which are compatible with an almost “perfect fluid” behavior, i.e. a small ratio of  $\eta/s$  [49–51].

The hydrodynamical description of the QGP medium created is validated by assuming the quasi-perfect fluid behavior [52, 53]. In the reaction process hypothesis, an intermediate stage, such as a boost-invariant QGP phase modeled as a relativistically expanding fluid, which constitutes the foundation of the Bjorken flow. In the central region of the collision, boost-invariance is justified by the flatness of the observed particle distribution. This observation agrees with hydrodynamic predictions of boost invariance, in which the fluid (space-time) rapidity equals with the particle (energy-momentum) rapidity [54].

In this work, we perform a systematic study of the Bjorken initial energy density. A generalized elliptic transverse overlap geometry is considered that remains valid from central to peripheral collisions. Using the es-

timated initial conditions, we study the subsequent longitudinal expansion of the QGP medium within the framework of boost-invariant relativistic hydrodynamics. Both ideal and first-order viscous hydrodynamics are investigated to check the effects of viscosity on the energy density evolution, entropy production, and lifetime of the QGP.

The paper is organized as follows. The formulation of the Bjorken model is discussed in Sec. II. The overlapping area calculation and initial condition estimations are done in Sec. III A and III B, respectively. In Sec. III C, we present the hydrodynamic evolution of the system. The resulting energy density evolution, viscous effects, entropy production, and QGP lifetime are analyzed in detail in Sec. IV. At the end of Sec. IV, a comparative study of Xe-Xe and Pb-Pb collisions is presented to highlight system-size and collision energy dependence. Finally, the main conclusions are summarized in Sec. V.

## II. BJORKEN MODEL

The hydrodynamic description introduced by Bjorken is one of the principal models used to describe the heavy-ion collisions at high energies [54]. The popular Bjorken flow, which is the boost invariant fluid flow does not depend on rapidity but only on proper time ( $\tau$ ) [55, 56]. In high-energy heavy-ion collisions at central rapidity, this phenomenological assumption holds true. This model has been very successful in describing the extreme regime, where velocity of fluid is close to the light velocity and is one of the simplest models. The space-time evolution of highly energetic and dense state of matter created in heavy-ion collisions is described by the Bjorken flow as an ultra-relativistic fluid [57, 58]. All the interesting dynamics takes place along the direction in which the collision of the two heavy nuclei occur i.e. along the beam axis, which is usually taken as  $z$ -axis. This is considered as one among the major simplifying assumptions of Bjorken flow. In the transverse  $x - y$  plane, the flow expects complete rotational and translational invariance, which leads it to become effectively two dimensional. The boost or to be more precise rapidity invariance, which claims about the existence of the velocity profile of the produced fluid after the collision, is the second major assumption of the Bjorken flow. The longitudinal velocity of the fluid at the location  $z$  is given by  $v = \frac{z}{t}$ , after assuming that the collision occurred at  $z = 0$  and at time  $t = 0$ . However, at any later time  $t$  the fluid exactly in the midway between the two receding nuclei continues to be at rest. This can also be interpreted as, the fluid at  $z = 0$  is at rest at a particular instant in time  $t$ , whereas the fluid is moving with the speed of light at  $z = \pm t$ . Assuming the QGP medium as a fluid system, the initial energy density is given by [54]:

$$\varepsilon_B = \frac{3}{2} \frac{dN_{ch}}{dy} \frac{\langle m_T \rangle}{\tau_o A_{overlap}} , \quad (1)$$

where  $\langle m_T \rangle$  is the transverse mass of the produced particles,  $\frac{dN_{ch}}{dy}$  being the charged particle rapidity density measured in relativistic heavy-ion collisions,  $\tau_0$  is the formation time of possible hydrodynamical system or initial time of a possible hydrodynamic evolution.  $A_{\text{overlap}}$  is the area of transverse overlapping region. According to this model an initial energy density  $\varepsilon_B \geq 1 \text{ GeV/fm}^3$  ensures the existence of the QGP medium.

### III. METHODOLOGY

#### A. Area of Overlapping Region

In the Bjorken picture, the transverse overlap area is conventionally approximated as a circular region, which is applicable for the most central collisions. To study with mid-central and most-peripheral collisions, the overlapping region is generalized by considering it as an elliptic geometry as shown in Fig. 1.

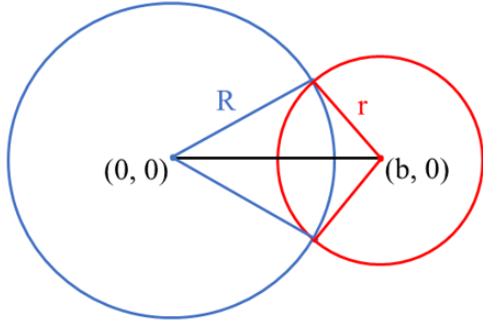


FIG. 1. Elliptic transverse overlap geometry formed in a non-central collision between two nuclei of radii  $R$  and  $r$  at impact parameter  $b$ .

The generalized overlapping area is calculated as,

$$A_{\text{overlap}} = R^2 \cos^{-1} \left( \frac{b^2 - r^2 + R^2}{2bR} \right) + r^2 \cos^{-1} \left( \frac{b^2 + r^2 - R^2}{2br} \right) - \frac{1}{2} \sqrt{(b+r+R)(b-r+R)(r+b-R)(r-b+R)}, \quad (2)$$

where  $R, r$  are the radii of the participating nuclei and  $b$  is the impact parameter. The radius of the Xe nucleus is calculated as  $R = R_0 A^{1/3}$ , where  $R_0$  is the Fermi radius ( $\sim 1.2 \text{ fm}$ ) and  $A$  is the mass number of the nucleus. This expression has been derived in detail in Appendix A. As a special case of this, if we take collision between two identical nuclei, i.e.  $R = r$ , then we get

$$A_{\text{overlap}} = 2R^2 \cos^{-1} \left( \frac{b}{2R} \right) - \frac{b}{2} \sqrt{4R^2 - b^2}. \quad (3)$$

The consistency of Eq. (3) can be checked by the fact that it correctly reproduces the limiting cases of complete overlap and vanishing overlap at  $b = 0$  and  $b = 2R$ , respectively.

The calculated overlap area is then investigated as a function of the number of participating nucleons  $N_{\text{part}}$  for Xe-Xe and Pb-Pb collisions, as shown in Fig. 2. The overlap area increases monotonically with increase in  $N_{\text{part}}$  for both systems.

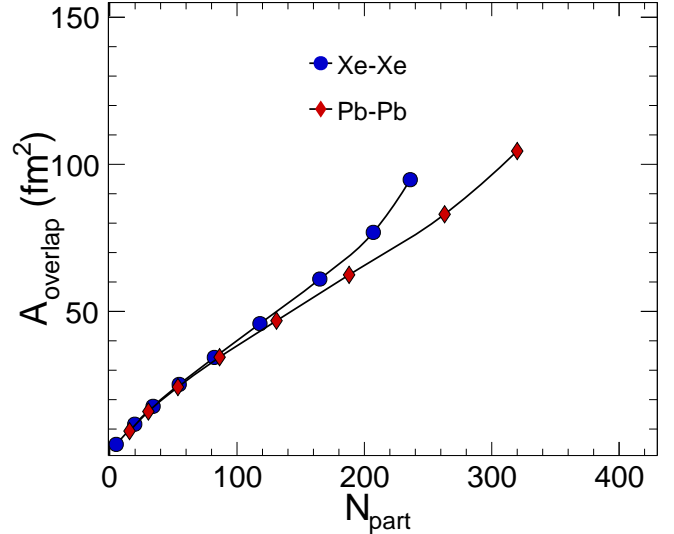


FIG. 2. Generalized elliptic overlap area  $A_{\text{overlap}}$  as a function of the number of participating nucleons  $N_{\text{part}}$  for Xe-Xe collisions at  $\sqrt{s_{NN}} = 5.44 \text{ TeV}$  and Pb-Pb collisions at  $\sqrt{s_{NN}} = 5.02 \text{ TeV}$ .

In the peripheral region, the overlap areas of the two collision systems are comparable. However, with increasing  $N_{\text{part}}$ , a clear system-size dependence becomes evident. For mid-central and central collisions, the overlap area in Xe-Xe collisions exceeds that in Pb-Pb collisions at comparable  $N_{\text{part}}$ . This implies that Pb-Pb collisions can accommodate the same number of participating nucleons as Xe-Xe collisions within a more compact transverse geometry, resulting in a higher participant density in Pb-Pb collisions. The area of overlapping  $A_{\text{overlap}}$  is an explicit input to the Bjorken initial energy density estimation. Consequently, these system size dependent differences in transverse geometry play a crucial role in the quantitative comparison of Bjorken initial energy densities, as discussed in the following sections.

#### B. Estimation of Bjorken Initial Energy Density

The Bjorken initial energy density is calculated for different centralities under two scenarios: a fixed formation time and varying  $\tau_0$ , using the Bjorken formula as given in Eq. (1). The average transverse mass ( $\langle m_T \rangle$ ) of pions is taken to be 0.562 GeV. The charged particle rapidity

density  $\left(\frac{dN_{ch}}{dy}\right)$  is taken from ALICE data [59].

In the fixed- $\tau_0$  scenario,  $\tau_0$  is set to 0.6 fm for all centrality classes. For Pb-Pb collisions at  $\sqrt{s_{NN}} = 5.02$  TeV,  $\varepsilon_B$  is calculated for the fixed- $\tau_0$  case in different centrality classes. However, in the varying  $\tau_0$  scenario,  $\tau_0$  is extracted using Eq. (1) from the published energy-density values of Pb-Pb collisions at  $\sqrt{s_{NN}} = 5.02$  TeV for different centralities. For Xe-Xe collisions at  $\sqrt{s_{NN}} = 5.44$  TeV, the Bjorken initial energy density ( $\varepsilon_B$ ) is evaluated for both scenarios across all centrality classes.

### C. Hydrodynamic Evolution Framework

The space-time evolution of the QGP medium formed in Xe-Xe collisions at  $\sqrt{s_{NN}} = 5.44$  TeV is studied within the framework of relativistic hydrodynamics. In this work, we focus on the longitudinal expansion of the system under the assumption of boost invariance in the transverse directions. We restrict our study to ideal and first-order viscous hydrodynamics.

The energy-momentum tensor for a locally thermalized relativistic viscous fluid is given by,

$$T^{\alpha\beta} = \varepsilon u^\alpha u^\beta - P \Delta^{\alpha\beta} + \xi^{\alpha\beta} + \Delta^{\alpha\beta} \zeta, \quad (4)$$

where  $\varepsilon$  is energy density,  $u^\mu = (\gamma, \gamma \vec{v})$  is four-velocity of the fluid cell with  $\gamma$  being the Lorentz factor,  $P$  is the pressure.  $\Delta^{\alpha\beta} = g^{\alpha\beta} - u^\alpha u^\beta$  is the projection operator with the metric tensor  $g^{\alpha\beta} = \text{diag}(1, -1, -1, -1)$ .  $\xi^{\alpha\beta}$  represents shear viscous correction, and  $\Delta^{\alpha\beta} \zeta$  corresponds to bulk viscous correction. At high temperature, the QGP medium is approximately conformal; therefore, the contribution from bulk viscosity is neglected throughout this study [60]. In the absence of viscous correction terms, Eq. (4) reduces to the ideal energy-momentum tensor.

In first-order hydrodynamic framework, shear stress tensor is expressed as,

$$\xi^{\alpha\beta} = 2\eta \lambda^{\alpha\beta}, \quad (5)$$

where  $\eta$  is the shear viscosity, with

$$\lambda^{\alpha\beta} = \frac{1}{2} (\nabla^\alpha u^\beta + \nabla^\beta u^\alpha) - \frac{1}{3} \Delta^{\alpha\beta} (\nabla \cdot u), \quad (6)$$

where  $\nabla^\alpha = \partial^\alpha - u^\alpha u^\rho \partial_\rho$  is the covariant derivative.

The hydrodynamic evolution is governed by local energy-momentum conservation,

$$\partial_\alpha T^{\alpha\beta} = 0. \quad (7)$$

To extract the energy evolution equation independent of momentum dynamics, we project Eq. (7) along the fluid velocity, i.e.  $u_\beta \partial_\alpha T^{\alpha\beta} = 0$ . We then simplify this expression to obtain the corresponding rate equations. For this purpose, we consider the ideal and viscous contributions separately.

#### 1. Ideal case

The ideal part of  $u_\beta \partial_\alpha T^{\alpha\beta}$  includes only the first two terms in  $T^{\alpha\beta}$ , which gives

$$\begin{aligned} u_\beta \partial_\alpha [\varepsilon u^\alpha u^\beta - P \Delta^{\alpha\beta}] \\ = \partial_\alpha ((\varepsilon + P) u^\alpha) - u_\beta g^{\alpha\beta} \partial_\alpha P, \end{aligned} \quad (8)$$

which is obtained using  $u_\beta u^\beta = 1$ ,  $u_\beta (\partial_\alpha u^\beta) = 0$ , and  $u_\beta \Delta^{\alpha\beta} = 0$ .

In this study, we consider a simple 1 + 1 dimensional case. The fluid has only longitudinal velocity, which is assumed to be  $v_z = \frac{z}{\tau}$  with  $z$  and  $\tau$  as longitudinal direction and proper time, respectively.

To simplify Eq. (8) further we use  $\partial_\alpha u^\alpha = \frac{1}{\tau}$  and  $u^\alpha \partial_\alpha = \frac{\partial}{\partial \tau}$ , which are derived explicitly in Appendix B and C respectively. The simplification leads us to

$$u_\beta \partial_\alpha [\varepsilon u^\alpha u^\beta - P \Delta^{\alpha\beta}] = \frac{d\varepsilon}{d\tau} + \frac{\varepsilon + P}{\tau}. \quad (9)$$

#### 2. Viscous case

In case of viscous contributions, the third term in  $T^{\alpha\beta}$  contained in the expression  $u_\beta \partial_\alpha T^{\alpha\beta}$  is considered. We have chosen Landau frame where the viscous stress does not transport energy in the local rest frame. Consequently, the transversality of the shear stress tensor implies  $u_\beta \xi^{\alpha\beta} = 0$ . The detailed derivation is explicitly shown in Appendix D. Using this condition, we obtain,

$$u_\beta \partial_\alpha \xi^{\alpha\beta} = -\xi^{\alpha\beta} \partial_\alpha u_\beta = -2\eta \lambda^{\alpha\beta} \partial_\alpha u_\beta. \quad (10)$$

Further simplification of this expression, explicitly derived in Appendix E, gives

$$u_\beta \partial_\alpha \xi^{\alpha\beta} = \frac{4\eta}{3\tau^2}. \quad (11)$$

By combining the ideal and viscous contributions, the rate equation for the energy density becomes

$$\frac{d\varepsilon}{d\tau} = -\frac{\varepsilon + P}{\tau} + \frac{4\eta}{3\tau^2}, \quad (12)$$

which reproduces the ideal rate equation in the limit  $\eta = 0$ . For the present study, we use a conformal equation of state and the pressure, therefore becomes  $P = \frac{\varepsilon}{3}$ .

From relativistic kinetic theory, it has been observed that the shear viscosity primarily depends on  $\frac{\varepsilon}{T}$  [61]. Hence, we can reasonably approximate  $\eta$  as  $\eta \approx \kappa \frac{\varepsilon}{T}$ , with a weakly temperature dependent coefficient  $\kappa$ . In the subsequent calculations,  $\kappa$  is treated as a constant parameter. Now the rate equation for shear viscosity becomes

$$\frac{d\eta}{d\tau} = \frac{\kappa}{T} \frac{d\varepsilon}{d\tau} \left(1 - \frac{\varepsilon}{4aT^4}\right), \quad (13)$$

where we have used the relation  $\varepsilon = aT^4$  with the constant  $a = \frac{\pi^2}{30} (16 + 10.5N_f)$ . In this study, we have considered the plasma containing massless  $u$ ,  $d$ ,  $s$  quarks, and number of quark flavors,  $N_f = 3$ . Simplification of Eq. (13) leads to,

$$\frac{d\eta}{d\tau} = \frac{3\eta}{4\varepsilon} \frac{d\varepsilon}{d\tau}. \quad (14)$$

Eqs. (12) and (14) are two coupled differential equations. Both these equations are simultaneously solved numerically to obtain the space-time evolution of the energy density and shear viscosity.

## IV. RESULTS

### A. Estimation of Bjorken Initial Energy Density ( $\varepsilon_B$ )

We have calculated the Bjorken initial energy density ( $\varepsilon_B$ ) for different centrality classes in Xe-Xe collisions at  $\sqrt{s_{NN}} = 5.44$  TeV for both fixed  $\tau_0$  and varying  $\tau_0$  cases. For Pb-Pb collisions at  $\sqrt{s_{NN}} = 5.02$  TeV, the  $\varepsilon_B$  values for different centrality classes are evaluated only for fixed  $\tau_0$  case. In the fixed- $\tau_0$  case,  $\tau_0$  is set to 0.6 fm for all the centrality classes. The area of overlap region  $A_{\text{overlap}}$  is calculated by using Eq. (3) and along with the corresponding Bjorken initial energy density values obtained from Eq. (1) for different centrality classes in Xe-Xe collisions at  $\sqrt{s_{NN}} = 5.44$  TeV, are shown in Table I. The Bjorken initial energy density ( $\varepsilon_B$ ) values calculated for different centrality classes in Pb-Pb collisions at  $\sqrt{s_{NN}} = 5.02$  TeV are shown in Table II.

In the varying  $\tau_0$  scenario, the formation time  $\tau_0$  for different centrality classes is extracted from the published energy density ( $\varepsilon_B$ ) values for Pb-Pb collisions at  $\sqrt{s_{NN}} = 5.02$  TeV using Eq. (1). The extracted  $\tau_0$  values, along with the corresponding area of overlap region  $A_{\text{overlap}}$  calculated by using Eq. (3) and the published Bjorken initial energy density ( $\varepsilon_B$ ) values from ALICE data for different centrality classes in Pb-Pb collisions at  $\sqrt{s_{NN}} = 5.02$  TeV are shown in Table III. The area of overlap region  $A_{\text{overlap}}$  and Bjorken initial energy density ( $\varepsilon_B$ ) values for different centrality classes are calculated in Xe-Xe collisions at  $\sqrt{s_{NN}} = 5.44$  TeV by using the  $\tau_0$  extracted from published energy density ( $\varepsilon_B$ ) values of Pb-Pb collisions at  $\sqrt{s_{NN}} = 5.02$  TeV, and are shown in Table IV.

The variation of the Bjorken initial energy density ( $\varepsilon_B$ ) with the number of participant nucleons ( $N_{\text{part}}$ ) for both the fixed  $\tau_0$  and varying  $\tau_0$  cases in Xe-Xe at  $\sqrt{s_{NN}} = 5.44$  TeV and Pb-Pb collisions at  $\sqrt{s_{NN}} = 5.02$  TeV is shown in Fig. 3. The Bjorken initial energy density increases monotonically with  $N_{\text{part}}$  for both of the colliding systems. This behavior is a direct consequence of the growth of the transverse overlap area and particle production with increase in collision centrality. The varying- $\tau_0$  scenario leads to comparatively lower  $\varepsilon_B$  values, especially in peripheral collisions. This behavior highlights the role

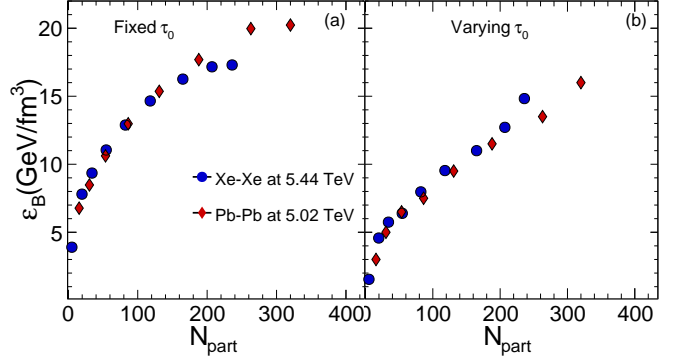


FIG. 3. Bjorken initial energy density  $\varepsilon_B$  as a function of  $N_{\text{part}}$  for Xe-Xe and Pb-Pb collisions under (a) fixed formation time  $\tau_0$  and (b) centrality dependent  $\tau_0$  scenarios.

of a centrality-dependent formation time in moderating the initial energy density, while preserving the overall  $N_{\text{part}}$  scaling.

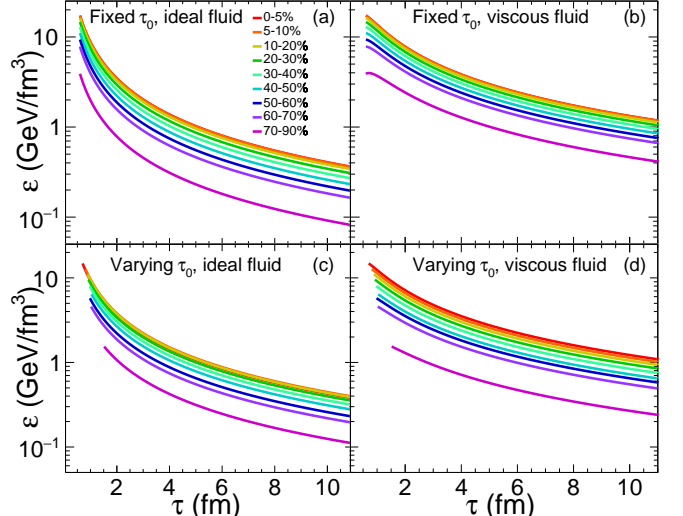


FIG. 4. Time evolution of energy density  $\varepsilon(\tau)$  for different centrality classes in Xe-Xe collisions at  $\sqrt{s_{NN}} = 5.44$  TeV for ideal and viscous hydrodynamics under fixed and varying  $\tau_0$  scenarios.

### B. Evolution of the QGP Medium

Using the Bjorken initial energy density ( $\varepsilon_B$ ) and the corresponding formation time  $\tau_0$  as initial conditions, the subsequent space-time evolution of the QGP medium formed in Xe-Xe collisions at  $\sqrt{s_{NN}} = 5.44$  TeV is studied by numerically solving the coupled hydrodynamic equations derived in Sec. III C. Both ideal and first-order viscous hydrodynamic evolution are studied under the assumption of boost-invariant longitudinal expansion.

TABLE I. Bjorken initial energy density ( $\varepsilon_B$ ) calculated by using the charged particle rapidity density  $\left(\frac{dN_{ch}}{dy}\right)$  [59], area of overlap region ( $A_{overlap}$ ), the formation time  $\tau_0$  as given in this table for different centrality classes in Xe-Xe collisions at  $\sqrt{s_{NN}} = 5.44$  TeV.

Centrality class (%)	$N_{part}$	$\frac{dN_{ch}}{d\eta}$	b (fm)	$A_{overlap,Cal}$ (fm) <sup>2</sup>	$\tau_0$ (fm)	$\varepsilon_{B,Cal}$ (GeV/(fm) <sup>3</sup> )
0-5	236	1167	1.817	94.778	0.600	17.299
5-10	207	939	3.320	76.868	0.600	17.163
10-20	165	706	4.698	61.004	0.600	16.260
20-30	118	478	6.086	45.830	0.600	14.653
30-40	82.2	315	7.209	34.352	0.600	12.883
40-50	54.6	198	8.179	25.178	0.600	11.049
50-60	34.1	118	9.042	17.727	0.600	9.352
60-70	19.7	64.7	9.829	11.650	0.600	7.802
70-90	5.13	13.3	10.900	4.790	0.600	3.901

TABLE II. Bjorken initial energy density ( $\varepsilon_B$ ) calculated by using the charged particle rapidity density  $\left(\frac{dN_{ch}}{dy}\right)$  [59], area of overlap region ( $A_{overlap}$ ) and the formation time  $\tau_0$  as given in this table for different centrality classes in Pb-Pb collisions at  $\sqrt{s_{NN}} = 5.02$  TeV.

Centrality class (%)	$N_{part}$	$\frac{dN_{ch}}{d\eta}$	b (fm)	$A_{Overlap,Cal}$ (fm) <sup>2</sup>	$\tau_0$ (fm)	$\varepsilon_{B,Cal}$ (GeV/(fm) <sup>3</sup> )
0-10	320	1505	3.867	104.510	0.600	20.232
10-20	263	1180	5.468	83.019	0.600	19.970
20-30	188	786	7.083	62.429	0.600	17.689
30-40	131	512	8.391	46.834	0.600	15.360
40-50	86.3	318	9.514	34.436	0.600	12.974
50-60	53.6	183	10.521	24.281	0.600	10.616
60-70	30.4	96.3	11.443	15.961	0.600	8.477
70-80	15.6	44.9	12.293	9.314	0.600	6.773

### 1. Longitudinal Evolution of Energy Density ( $\varepsilon$ )

Figure 4 shows the evolution of energy density for different centrality classes under two distinct scenarios: (i) varying  $\tau_0$ , where the formation time increases from central to peripheral collisions as extracted from Pb-Pb data at  $\sqrt{s_{NN}} = 5.02$  TeV, and (ii) a fixed  $\tau_0$ , where a constant value  $\tau_0 = 0.6$  fm is used for all centralities to isolate the role of initial time as a control parameter. In both scenarios, the energy density decreases monotonically with proper time, reflecting the longitudinal work performed by the expanding medium as the Co-moving volume increases. In the ideal case, the evolution follows Bjorken scaling  $\varepsilon \propto \tau^{-4/3}$  for conformal equation of state. With the inclusion of viscous effects, the dilution of energy density is reduced, leading to systematically higher energy densities at later times compared to the ideal case. This behavior arises from viscous contributions to the longitudinal pressure, which counteract the rapid dilution induced by longitudinal expansion.

To disentangle the effect of formation time  $\tau_0$  from that of the initial energy density  $\varepsilon_B$ , a fixed  $\tau_0$  scenario is considered as shown in Figs. 4(a, b). Although, this assumption is not realistic, it is considered to investigate the differences between centrality classes arising solely

from variations in  $\varepsilon_B$ , which are determined by collision geometry and particle production in the collisions.

Figures 4(c, d) show evolution of energy density in varying  $\tau_0$  scenario. In peripheral collisions, the hydrodynamic evolution begins at larger  $\tau_0$  with smaller initial energy density  $\varepsilon_B$ . Thus, these systems reach dilute conditions more rapidly and exhibit a shorter lifetime of the dense QGP phase. In contrast, central collisions are characterized by smaller  $\tau_0$  and larger  $\varepsilon_B$ , allowing the system to remain in the de-confined phase for a longer duration. The higher participant densities in central collisions favor faster local equilibrium, thereby justifying the earlier applicability of hydrodynamics. Comparison of the fixed and varying  $\tau_0$  cases indicates that a centrality dependent formation time enhances the contrast between central and peripheral collisions, particularly during the early stages of the evolution.

### 2. Evolution of Shear Viscosity ( $\eta$ )

Figure 5 shows proper time evolution of the shear viscosity  $\eta(\tau)$  for different centrality classes for both fixed and varying  $\tau_0$  scenarios. In all cases,  $\eta$  decreases monotonically with proper time ( $\tau$ ) reflecting the cooling of

TABLE III. The formation time  $\tau_0$  calculated by using the charged particle rapidity density  $\left(\frac{dN_{ch}}{dy}\right)$  [59], area of overlap region ( $A_{overlap}$ ) and the Bjorken initial energy density ( $\varepsilon_B$ ) as given in this table for different centrality classes in Pb-Pb collisions at  $\sqrt{s_{NN}} = 5.02$  TeV [62].

Centrality class (%)	$N_{part}$	$\frac{dN_{ch}}{dy}$	b (fm)	$A_{Overlap,Cal}(fm)^2$	$\tau_{0,Cal}(fm)$	$\varepsilon_{B,Pub} (GeV/(fm)^3)$
0-10	320	1505	3.867	104.510	0.758	16.000
10-20	263	1180	5.468	83.019	0.887	13.500
20-30	188	786	7.083	62.429	0.922	11.500
30-40	131	512	8.391	46.834	0.970	9.500
40-50	86.3	318	9.514	34.436	1.037	7.500
50-60	53.6	183	10.521	24.281	0.977	6.500
60-70	30.4	96.3	11.443	15.961	1.023	5.000
70-80	15.6	44.9	12.293	9.314	1.354	3.000

TABLE IV. Bjorken initial energy density ( $\varepsilon_B$ ) calculated by using the charged particle rapidity density  $\left(\frac{dN_{ch}}{dy}\right)$  [59], area of overlap region ( $A_{overlap}$ ), the formation time  $\tau_0$  as given in this table for different centrality classes in Xe-Xe collisions at  $\sqrt{s_{NN}} = 5.44$  TeV.

Centrality class (%)	$N_{part}$	$\frac{dN_{ch}}{dy}$	b (fm)	$A_{overlap,Cal} (fm)^2$	$\tau_{0,Cal} (fm)$	$\varepsilon_{B,Cal} (GeV/(fm)^3)$
0-5	236	1167	1.817	94.778	0.700	14.828
5-10	207	939	3.320	76.868	0.810	12.713
10-20	165	706	4.698	61.004	0.887	10.999
20-30	118	478	6.086	45.830	0.922	9.536
30-40	82.2	315	7.209	34.352	0.970	7.969
40-50	54.6	198	8.179	25.178	1.037	6.393
50-60	34.1	118	9.042	17.727	0.977	5.743
60-70	19.7	64.7	9.829	11.650	1.023	4.576
70-90	5.13	13.3	10.900	4.790	1.519	1.541

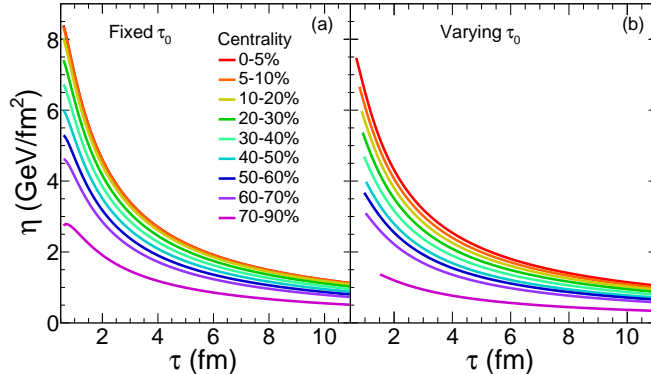


FIG. 5. Time evolution of shear viscosity  $\eta(\tau)$  for different centrality classes in Xe-Xe collisions for (a) fixed  $\tau_0$  and (b) centrality dependent  $\tau_0$  scenarios.

the system. Due to the longitudinal expansion of the medium, the temperature and energy density decrease with time, leading to a corresponding reduction in the magnitude of shear viscosity. Central collisions exhibit larger initial values of  $\eta$  and therefore sustain higher viscosity over a longer duration as compared to peripheral collisions, consistent with their larger  $\varepsilon_B$ .

Evolution of viscosity in fixed  $\tau_0$  case is shown in Fig. 5(a) where the ordering of  $\eta(\tau)$  across centrality classes is determined solely by collision geometry and particle production. The corresponding case of varying  $\tau_0$  is shown in Fig. 5(b). Peripheral collisions have smaller initial  $\eta$  values due to their significantly lower  $\varepsilon_B$  values causing viscous effects to become sub-dominant at relatively early times. In contrast, central collisions retain substantial viscous contributions during the early stages of evolution, which plays a crucial role in moderating the cooling rate and entropy generation, as discussed later in this study.

The evolution of  $\varepsilon$  and  $\eta$  gives a coherent description of the longitudinal dynamics of the QGP medium. In the following sections, we explore the implications of this evolution for entropy production and the effective lifetime of the disordered de-confined QGP medium.

To further elucidate the effect of shear viscosity on the dynamical evolution, a direct comparison between ideal and viscous fluid dynamics is performed for the most central (0 – 5%) and most peripheral (70 – 90%) centrality classes in Xe-Xe collisions. Shear viscosity contributes to the longitudinal pressure, which partially counterbalances the work done by the system during longitudinal expansion. As a result, the inclusion of shear viscosity

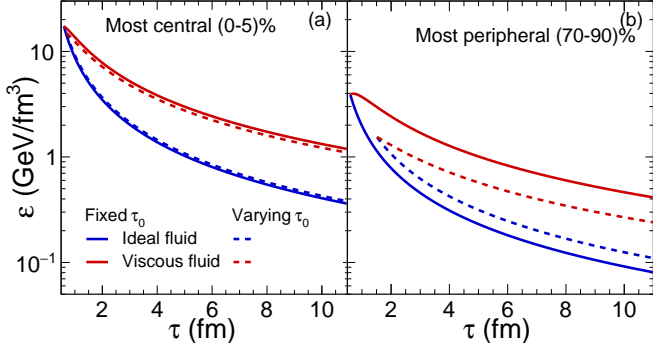


FIG. 6. Comparison of ideal and viscous energy density evolution for the most central (0 – 5%) and most peripheral (70 – 90%) Xe-Xe collisions under fixed and varying  $\tau_0$  assumptions.

leads to a systematically slower cooling of the medium compared to the ideal case, in both central and peripheral collisions. This is consistent for both fixed and centrality-dependent formation-time scenarios as shown in Fig. 6.

A clear distinction emerges in the most peripheral collisions, where viscous effects are significantly more pronounced in the fixed  $\tau_0$  case than in the varying  $\tau_0$  scenario. Upon fixing  $\tau_0$  for all centralities we force peripheral collisions to undergo local equilibrium at an early proper time despite their lower  $\varepsilon_B$  value. At such early times the longitudinal expansion rate is large, which enhances the relative contribution of the viscous terms to the evolution equations and resulting in an artificially strong viscous correction in the most peripheral collisions. However, in the case of varying  $\tau_0$ , onset of evolution happens at larger formation time. This delay reduces the effective expansion rate and suppresses viscous corrections, leading to a much smaller deviation between ideal and viscous evolution, as shown in Fig. 6(b). This behavior is expected, as dilute systems are supposed to thermalize later and undergo a shorter viscous hydrodynamic phase.

In the most central collisions, as shown in Fig. 6(a), the effect of viscosity is more pronounced. Here as well, fixing  $\tau_0$  tends to overestimate the viscous corrections as compared to the more realistic centrality-dependent  $\tau_0$  case. However, due to smaller  $\tau_0$  and higher  $\varepsilon_B$  values in central collisions for both the cases, the quantitative differences between fixed and varying  $\tau_0$  cases remains small.

### 3. Entropy production in Longitudinal Expansion

The same mechanism is reflected in the entropy production during evolution, as shown in Fig. 7. For an ideal fluid undergoing boost-invariant longitudinal expansion, entropy per unit rapidity is conserved. Therefore, the ratio  $s(\tau)\tau/s(\tau_0)\tau_0$  remains constant throughout the evolution for different cases of ideal fluid. In

contrast, the viscous evolution exhibits a monotonic increase of this ratio, reflecting entropy production due to shear viscosity. This entropy generation is most significant at the early stages of the evolution, when velocity gradients are largest. Then the ratio gradually saturates at later times as the medium cools and the expansion rate decreases. A noteworthy observation from Fig. 7

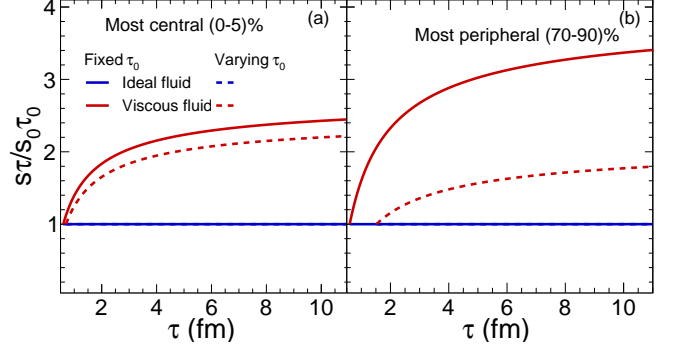


FIG. 7. Entropy production quantified through dimensionless  $s(\tau)\tau/s(\tau_0)\tau_0$  for ideal and viscous evolution in central and peripheral Xe-Xe collisions.

is that, in the viscous case, the centrality-dependent  $\tau_0$  scenario results in smaller total entropy production as compared to fixed  $\tau_0$  case in both central and peripheral collisions. This behavior is a direct consequence of the delayed onset of hydrodynamic evolution in varying  $\tau_0$  case, particularly for peripheral collisions. Since entropy production is dominated by early stages of evolution, initiating the hydrodynamics at a larger formation time effectively reduces the interval over which dissipative processes act, thereby leads to a smaller increase in entropy. In contrast, the fixed  $\tau_0$  case systematically overestimates the entropy production. This overestimation is more pronounced in the most peripheral collisions, where the medium is forced to start undergoing evolution at earlier formation time with low initial energy density. These observations establish a clear correlation between the slower energy density evolution in viscous hydrodynamics and the associated entropy production.

### 4. Lifetime of the QGP Medium

The hydrodynamic evolution discussed in the preceding sections allows us to estimate the effective lifetime of the QGP medium formed in Xe-Xe collisions at  $\sqrt{s_{NN}} = 5.44$  TeV. Within the Bjorken framework, the QGP phase is assumed to persist as long as the energy density remains above a critical value. Following standard phenomenological practice, we take the critical energy density as  $\varepsilon_c = 1$  GeV/fm<sup>3</sup> for the onset of hadronization. The proper time at which  $\varepsilon$  drops below this threshold is defined as lifetime of QGP, denoted by  $\tau_{\text{critical}}$ .

Figure 8 shows the QGP lifetime as a function of the number of participating nucleons  $N_{\text{part}}$ , for both ideal

and viscous case for both varying and fixed  $\tau_0$  scenarios. The lifetime increases monotonically with increasing  $N_{\text{part}}$ . Central collisions, characterized by larger overlap area and higher  $\varepsilon_B$ , remain longer in the de-confined phase whereas peripheral collisions cool more rapidly and undergo earlier hadronization. This trend reflects stronger longitudinal dilution exhibited by smaller and more dilute systems and provides a consistency check of the Bjorken initial conditions and subsequent evolution. As discussed earlier, shear viscosity generates additional longitudinal pressure, which slows the cooling rate of the medium. Consequently,  $\varepsilon$  remains above 1 GeV/fm $^3$  for a longer time, leading to an increased lifetime of QGP.

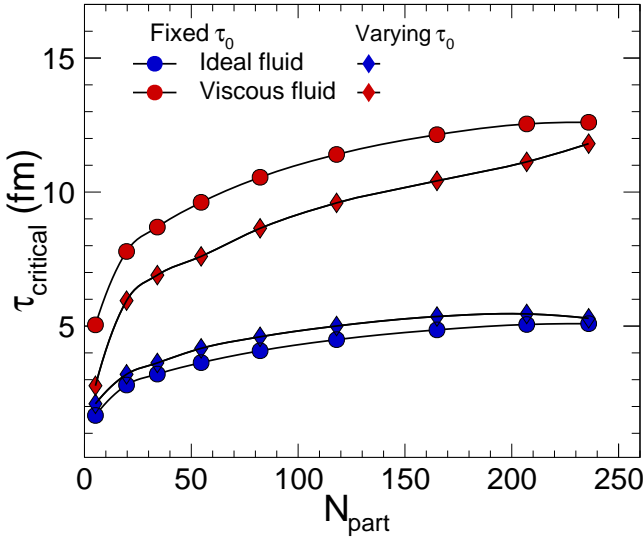


FIG. 8. Lifetime of the QGP phase  $\tau_{\text{critical}}$  (defined by  $\varepsilon = 1$  GeV/fm $^3$ ) as a function of  $N_{\text{part}}$  for ideal and viscous evolution under fixed and varying  $\tau_0$  scenarios.

The distinction between fixed and varying  $\tau_0$  cases is relatively small for ideal fluid. However, upon including viscosity the difference becomes substantial, particularly in peripheral collisions. This behavior can be understood from the structure of the hydrodynamic evolution equations in conjunction with the Bjorken initial condition. In ideal Bjorken flow, lifetime of the QGP exhibits a weak dependence on the formation time, scaling as  $\tau_{\text{critical}} \propto \tau_0^{1/4}$ . In contrast, the viscous term in the evolution equation scales as  $1/\tau^2$ , rendering the evolution sensitive to early-time dynamics. As a result, memory effects from the early stages strongly influence the extracted QGP lifetime in presence of viscosity.

In peripheral collisions, fixing  $\tau_0$  leads to an overestimation of the QGP lifetime by forcing the system to undergo early evolution with a reduced  $\varepsilon_B$ .

Upon employing a centrality-dependent formation time delays the onset of hydrodynamic evolution. This delayed onset suppresses early time viscous contributions, resulting in a much shorter and more realistic QGP lifetime. For the most central collisions, the values of  $\tau_0$  are small and comparable in both scenarios. Viscous ef-

fects act over a similar early time interval, thus the distinction between fixed and varying  $\tau_0$  scenarios remains modest.

### 5. Comparison of $\varepsilon$ Evolution in Xe-Xe and Pb-Pb Collisions

In this subsection, we compare the hydrodynamic evolution of the QGP medium formed in Xe-Xe collisions at  $\sqrt{s_{NN}} = 5.44$  TeV with that in Pb-Pb collisions at  $\sqrt{s_{NN}} = 5.02$  TeV. This study investigates the dependence of the evolution on the colliding system and the collision energy within the Bjorken framework.

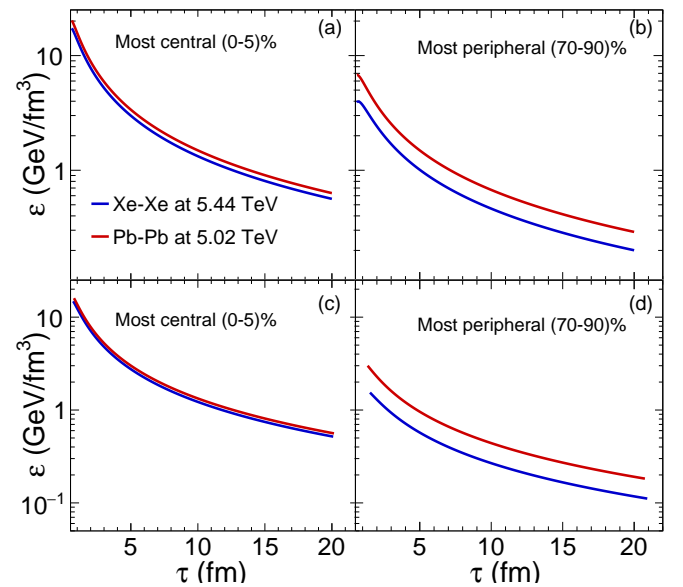


FIG. 9. Comparison of longitudinal energy density evolution in Xe-Xe and Pb-Pb collisions for most central and peripheral events. Top panels show fixed  $\tau_0$  case and bottom panels show the varying  $\tau_0$  case.

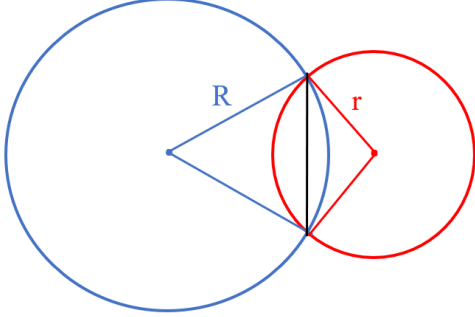
For the most central collisions, as shown in Figs. 9(a, c), the energy density evolution in Pb-Pb collisions remains systematically higher than that in Xe-Xe collisions for both fixed and varying  $\tau_0$  cases. This difference is attributed to the ratio of charged particle multiplicity to the effective Bjorken volume at the onset of the hydrodynamic evolution,  $((dN_{\text{ch}}/dy) / (A_{\text{overlap}}\tau_0))$ . The ratio value for Pb-Pb collisions is higher than that in Xe-Xe collisions, causing higher  $\varepsilon$  for the former. Figures 9(b, d) show the ordering observed for the most peripheral collisions. Here the separation between the two systems becomes more pronounced. This again depicts a direct correlation with the ordering of the multiplicity to volume ratio. Due to the larger relative differences among systems and energies, peripheral collisions provide a more sensitive environment for disentangling system-size and collisions-energy dependent effects in the longitudinal hydrodynamic evolution.

## V. SUMMARY

We study the Bjorken initial energy density ( $\varepsilon_B$ ) in Xe-Xe collisions at  $\sqrt{s_{NN}} = 5.44$  TeV using the Bjorken prescription. To quantify the role of formation time, both fixed and centrality-dependent  $\tau_0$  cases are considered. The centrality dependence of the  $\varepsilon_B$  is studied using a generalized and more realistic elliptic transverse overlap geometry, extending the conventional circular approximation to mid-central and peripheral collisions. Using the initial energy density ( $\varepsilon_B$ ) and formation time ( $\tau_0$ ), viscous longitudinal hydrodynamic evolution of the system formed in heavy-ion collisions is examined. We find that the formation time strongly influences the magnitude and centrality dependence of the initial energy density, with particularly pronounced effects in peripheral collisions. The inclusion of shear viscosity slows the longitudinal expansion and enhances entropy production. These viscous effects, dominated by early-time dynamics, are amplified when a fixed formation time is imposed, especially in peripheral collisions. In contrast, a centrality-dependent formation time reduces both viscous corrections and entropy production by delaying the onset of hydrodynamic evolution in dilute systems. The lifetime of quark-gluon plasma ( $\tau_{\text{critical}}$ ) increases with centrality and is further extended by the inclusion of viscosity in the model. To investigate the system-size dependence, results from Xe-Xe collisions are compared with those from Pb-Pb collisions at  $\sqrt{s_{NN}} = 5.02$  TeV. For the most central collisions, the energy densities and their time evolution are found to be nearly identical for both Xe-Xe and Pb-Pb collisions. In contrast, peripheral Pb-Pb collisions exhibit systematically higher energy densities compared to peripheral Xe-Xe collisions.

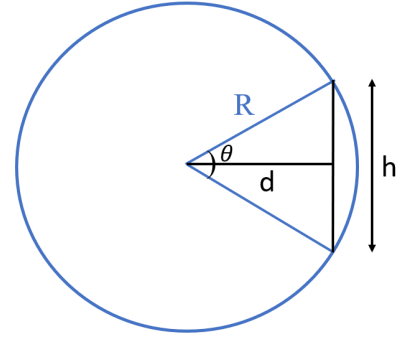
### Appendix A: Overlapping Area Calculation

The transverse overlapping area is equal to the sum of the areas of two circular segments, corresponding to participating nuclei.



The area of the circular segment of a nucleus can be found in the following way.

If we subtract the area of the triangle from the area of the circular sector, we will get the area of the circular



segment corresponding to the nucleus of radius  $R$ ,  $A_{cs}^R$ .

$$A_{cs}^R = \frac{1}{2}R^2\theta - \frac{1}{2}dh. \quad (\text{A1})$$

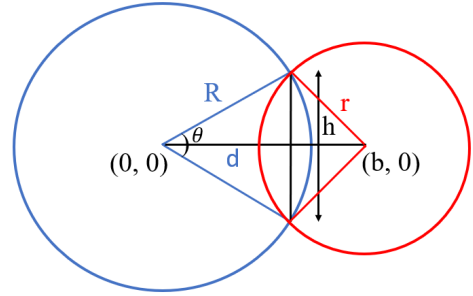
Using few simple trigonometric tricks, the last expression is simplified as,

$$A_{cs}^R = R^2 \cos^{-1} \left( \frac{d}{R} \right) - d\sqrt{R^2 - d^2}. \quad (\text{A2})$$

Similarly, area of circular segment corresponding to nucleus of radius  $r$ ,  $A_{cs}^r$  is written as,

$$A_{cs}^r = r^2 \cos^{-1} \left( \frac{b-d}{r} \right) - (b-d)\sqrt{r^2 - (b-d)^2}. \quad (\text{A3})$$

Now equation of two circular nuclei can be written as,



$$x^2 + y^2 = R^2, \quad \text{and} \quad (x - b)^2 + y^2 = r^2. \quad (\text{A4})$$

Solving these two equations we get,

$$x = \frac{b^2 - r^2 + R^2}{2b},$$

$$y = \frac{1}{2b} \sqrt{(b+R+r)(b+R-r)(r+b-R)(r-b+R)}. \quad (\text{A5})$$

It is easy to recognize that  $x = d$  and  $y = \frac{h}{2}$ . Now the overlapping area can be found as,

$$A_{\text{overlap}} = A_{cs}^R + A_{cs}^r, \quad (\text{A6})$$

$$A_{\text{overlap}} = R^2 \cos^{-1} \left( \frac{x}{R} \right) + r^2 \cos^{-1} \left( \frac{b-x}{r} \right) - x \sqrt{R^2 - x^2} - (b-x) \sqrt{r^2 - (b-x)^2}.$$

Using Eq. (A4), the last two terms in the expression can be simplified to give  $-by$ . So the final expression of the overlapping area becomes,

$$A_{\text{overlap}} = R^2 \cos^{-1} \left( \frac{b^2 - r^2 + R^2}{2bR} \right) + r^2 \cos^{-1} \left( \frac{b^2 + r^2 - R^2}{2br} \right) - \frac{1}{2} \sqrt{(b+r+R)(b-r+R)(r+b-R)(r-b+R)}. \quad (\text{A7})$$

## Appendix B: Calculation of $\partial_\alpha u^\alpha$

Milne coordinates provide a more physical efficient framework to describe the boost-invariant rapid longitudinal expansion of the medium formed in heavy-ion collisions. Calculations get simpler by allowing the system to evolve in proper time with simple flow fields and conservation equations. Hence for all the subsequent calculations, we will consider Milne coordinates given by  $\tau = \sqrt{t^2 - z^2}$ ,  $x = x$ ,  $y = y$  and  $\eta_s = \frac{1}{2} \ln \left( \frac{t+z}{t-z} \right)$ .  $\eta_s$  is the space-time rapidity. These relations can easily be inverted to give

$$t(\tau, \eta_s) = \tau \cosh \eta_s, \quad z(\tau, \eta_s) = \tau \sinh \eta_s. \quad (\text{B1})$$

And the conversion of partial derivatives are given by,

$$\frac{\partial}{\partial t} = \cosh \eta_s \frac{\partial}{\partial \tau} - \frac{\sinh \eta_s}{\tau} \frac{\partial}{\partial \eta_s}, \quad (\text{B2})$$

$$\frac{\partial}{\partial z} = -\sinh \eta_s \frac{\partial}{\partial \tau} + \frac{\cosh \eta_s}{\tau} \frac{\partial}{\partial \eta_s}. \quad (\text{B3})$$

The terms containing  $\sinh \eta_s$  as coefficient in above partial derivatives can be equated to zero, as at the end we will take mid-rapidity approximation which is  $\eta_s \rightarrow 0$ . Now, the four-velocity  $u^\alpha = \gamma(1, 0, 0, z/\tau) = \gamma(1, 0, 0, \sinh \eta_s)$ . Then the Lorentz factor  $\gamma = \frac{1}{\sqrt{1 - \sinh^2 \eta_s}}$ . With all these information in hand, we evaluate,

$$\begin{aligned} \partial_\alpha u^\alpha &= \frac{\partial}{\partial t} \gamma + \frac{\partial}{\partial z} \frac{\gamma z}{\tau} \\ &= \cosh \eta_s \frac{\partial \gamma}{\partial \tau} + \frac{\cosh \eta_s}{\tau} \frac{\partial}{\partial \eta_s} (\gamma \sinh \eta_s). \end{aligned}$$

Then in the limit  $\eta_s \rightarrow 0$ ,

$$\partial_\alpha u^\alpha = \frac{1}{\tau}. \quad (\text{B4})$$

## Appendix C: Calculation of $u^\alpha \partial_\alpha$

$$\begin{aligned} u^\alpha \partial_\alpha &= \gamma \frac{\partial}{\partial t} + \frac{\gamma z}{\tau} \frac{\partial}{\partial z} \\ &= \gamma \cosh \eta_s \frac{\partial}{\partial \tau} + \frac{\gamma \sinh \eta_s \cosh \eta_s}{\tau} \frac{\partial}{\partial \eta_s} \end{aligned}$$

Again in the mid-rapidity region,

$$u^\alpha \partial_\alpha = \frac{\partial}{\partial \tau}. \quad (\text{C1})$$

## Appendix D: Calculation of $u_\beta \xi^{\alpha\beta} = 0$

$$u_\beta \xi^{\alpha\beta} = 2\eta u_\beta \lambda^{\alpha\beta}. \quad (\text{D1})$$

Thus it is sufficient to show that  $u_\beta \lambda^{\alpha\beta}$  vanishes.

$$u_\beta \lambda^{\alpha\beta} = \frac{1}{2} (u_\beta \nabla^\alpha u^\beta + u_\beta \nabla^\beta u^\alpha) - \frac{1}{3} u_\beta \Delta^{\alpha\beta} (\nabla \cdot u). \quad (\text{D2})$$

The last term vanishes which is a direct result from the definition of the projection operator.

Now the first term,

$$u_\beta (\nabla^\alpha u^\beta) = \frac{1}{2} \nabla^\alpha (u_\beta u^\beta) = 0. \quad (\text{D3})$$

The second term,

$$u_\beta \nabla^\beta u^\alpha = u^\beta \nabla_\beta u^\alpha \equiv a^\alpha, \quad (\text{D4})$$

where  $a^\mu$  is the four-acceleration of the fluid cell. But we are considering Bjorken flow, which corresponds to geodesic motion. Hence the fluid cells follow straight worldlines in space-time, thus they don't have any proper acceleration. Hence the second term also vanishes. Summing contributions from all three terms we get,

$$u_\beta \xi^{\alpha\beta} = 0. \quad (\text{D5})$$

## Appendix E: Calculation of $u_\beta \partial_\alpha \xi^{\alpha\beta}$

$$u_\beta \partial_\alpha \xi^{\alpha\beta} = -2\eta \lambda^{\alpha\beta} \partial_\alpha u_\beta. \quad (\text{E1})$$

In Milne coordinates, i.e.  $x^\alpha = (\tau, x, y, \eta_s)$ , the metric tensor becomes,

$$g^{\alpha\beta} = \text{diag}(1, -1, -1, -\tau^{-2}), \quad g_{\alpha\beta} = \text{diag}(1, -1, -1, -\tau^2). \quad (\text{E2})$$

And nonzero Christoffel symbols,

$$\Gamma_{\eta_s \eta_s}^\tau = \tau, \quad \Gamma_{\tau \eta_s}^{\eta_s} = \Gamma_{\eta_s \tau}^{\eta_s} = \frac{1}{\tau}. \quad (\text{E3})$$

Now considering Bjorken flow in Milne coordinate, i.e. the velocity profile  $u^\alpha = u_\alpha = (1, 0, 0, 0)$ , we calculate

- Velocity gradients:

$$\nabla_\alpha u_\beta = \partial_\alpha u_\beta - \Gamma_{\alpha\beta}^\rho u_\rho = -\Gamma_{\alpha\beta}^\tau. \quad (\text{E4})$$

Hence the only nonzero component is

$$\nabla_{\eta_s} u_{\eta_s} = -\tau. \quad (\text{E5})$$

Now raising indices we get,

$$\nabla^{\eta_s} u^{\eta_s} = g^{\eta_s \eta_s} g^{\eta_s \eta_s} \nabla_{\eta_s} u_{\eta_s} = (-\tau^{-2}) (-\tau^{-2}) (-\tau) = -\frac{1}{\tau^3}. \quad (\text{E6})$$

Now, realizing the projection tensor as  $\Delta^{\alpha\beta} = \text{diag}(0, -1, -1, -\tau^{-2})$ , and using Eqs. (E6, E8) we write,

All other components of  $\nabla^\alpha u^\beta$  vanish.

- Expansion scalar:

$$\nabla \cdot u = \nabla_\alpha u^\alpha = \partial_\alpha u^\alpha + \Gamma_{\alpha\rho}^\alpha u^\rho. \quad (\text{E7})$$

The only nonzero term that survives is  $\nabla_{\eta_s} u^{\eta_s} = \Gamma_{\eta_s \tau}^{\eta_s} u^\tau = \frac{1}{\tau}$ . So,

$$\nabla \cdot u = \frac{1}{\tau}. \quad (\text{E8})$$

$$-2\eta \lambda^{\alpha\beta} \partial_\alpha u_\beta = -2\eta \lambda^{\eta_s \eta_s} \partial_\alpha u_\beta = \frac{4\eta}{3\tau^2}. \quad (\text{E9})$$

---

[1] E. Shuryak, *Rev. Mod. Phys.* **89**, 035001 (2017).

[2] J. Rafelski and B. Muller, *Phys. Rev. Lett.* **48**, 1066 (1982), [Erratum: *Phys. Rev. Lett.* **56**, 2334 (1986)].

[3] P. Koch, B. Muller, and J. Rafelski, *Phys. Rept.* **142**, 167 (1986).

[4] P. Koch, B. Muller, H. Stoecker, and W. Greiner, *Mod. Phys. Lett. A* **3**, 737 (1988).

[5] E. V. Shuryak, *Phys. Lett. B* **78**, 150 (1978).

[6] K. Adcox *et al.* (PHENIX), *Nucl. Phys. A* **757**, 184 (2005).

[7] R. Bellwied (STAR), *Nucl. Phys. A* **752**, 398 (2005).

[8] B. Muller and J. L. Nagle, *Ann. Rev. Nucl. Part. Sci.* **56**, 93 (2006).

[9] M. Gyulassy and L. McLerran, *Nucl. Phys. A* **750**, 30 (2005).

[10] S. Pal, *Phys. Lett. B* **684**, 211 (2010).

[11] M. J. Tannenbaum, *Rept. Prog. Phys.* **69**, 2005 (2006).

[12] H. Song and U. W. Heinz, *Phys. Lett. B* **658**, 279 (2008).

[13] K. Aamodt *et al.* (ALICE), *Phys. Rev. Lett.* **105**, 252302 (2010).

[14] G. Aad *et al.* (ATLAS), *Phys. Lett. B* **707**, 330 (2012).

[15] D. E. Kharzeev, *Phys. Rev. D* **90**, 074007 (2014).

[16] J. Adam *et al.* (ALICE), *Nature Phys.* **13**, 535 (2017).

[17] V. Khachatryan *et al.* (CMS), *Phys. Lett. B* **765**, 193 (2017).

[18] S. J. B. J. D. Bjorken and A. S. Goldhaber, *Phys. Lett. B* **726**, 344 (2013).

[19] C. Aidala *et al.* (PHENIX), *Nature Phys.* **15**, 214 (2019).

[20] A. Bazavov *et al.*, *Phys. Rev. D* **85**, 054503 (2012).

[21] E. Laermann and O. Philipsen, *Ann. Rev. Nucl. Part. Sci.* **53**, 163 (2003).

[22] B. B. Back *et al.* (PHOBOS), *Nucl. Phys. A* **757**, 28 (2005).

[23] Z. Yang, Y. Sun, and L. W. Chen, *Phys. Rev. C* **109**, 054907 (2024).

[24] H. B. Meyer, *Phys. Rev. D* **76**, 101701 (2007).

[25] J. Grefa, M. Hippert, J. Noronha, J. Noronha-Hostler, I. Portillo, C. Ratti, and R. Rougemont, *Phys. Rev. D* **106**, 034024 (2022).

[26] D. Teaney, *Phys. Rev. C* **68**, 034913 (2003).

[27] S. Ryu, J. F. Paquet, C. Shen, G. S. Denicol, B. Schenke, S. Jeon, and C. Gale, *Phys. Rev. Lett.* **115**, 132301 (2015).

[28] P. Romatschke and U. Romatschke, *Phys. Rev. Lett.* **99**, 172301 (2007).

[29] H. Niemi, K. J. Eskola, and R. Paatelainen, *Phys. Rev. C* **93**, 024907 (2016).

[30] J. E. Bernhard, P. W. Marcy, C. E. Coleman-Smith, S. Huzurbazar, R. L. Wolpert, and S. A. Bass, *Phys. Rev. C* **91**, 054910 (2015).

[31] M. R. Heffernan, C. Gale, S. Jeon, and J. F. Paquet, *Phys. Rev. C* **109**, 065207 (2024).

[32] G. Nijs and W. van der Schee, *Phys. Rev. Lett.* **129**, 232301 (2022).

[33] J. E. Parkkila, A. Onnerstad, S. F. Taghavi, C. Mordasini, A. Bilandzic, M. Virta, and D. J. Kim, *Phys. Lett. B* **835**, 137485 (2022).

[34] A. K. Chaudhuri, *Phys. Lett. B* **681**, 418 (2009).

[35] A. K. Chaudhuri, *Phys. Rev. C* **82**, 047901 (2010).

[36] S. Prasad, N. Mallick, S. Tripathy, and R. Sahoo, *Phys. Rev. D* **107**, 074011 (2023).

[37] P. Bozek and W. Broniowski, *Phys. Rev. C* **85**, 044910 (2012).

[38] R. Samanta, S. Bhatta, J. Jia, M. Luzum, and J. Y. Ollitrault, *Phys. Rev. C* **109**, L051902 (2024).

[39] K. A. *et al.* (ALICE), *Phys. Rev. Lett.* **107**, 032301 (2011).

[40] A. A. *et al.* (PHENIX), *Phys. Rev. Lett.* **107**, 252301 (2011).

[41] S. C. *et al.* (CMS), *Phys. Rev. C* **89**, 044906 (2014).

[42] M. A. *et al.* (ATLAS), *JHEP* **01**, 051.

[43] U. Heinz and R. Snellings, *Ann. Rev. Nucl. Part. Sci.* **63**, 123 (2013).

[44] W. Broniowski, M. Chojnacki, and L. Obara, *Phys. Rev. C* **80**, 051902 (2009).

[45] J. Y. Ollitrault, *Phys. Rev. D* **46**, 229 (1992).

[46] A. K. Yadav, P. P. Bhaduri, and S. Chattopadhyay, *Eur. Phys. J. C* **85**, 247 (2025).

[47] C. Shen, U. Heinz, P. Huovinen, and H. Song, *Phys. Rev. C* **84**, 044903 (2011).

[48] T. Hirano, N. van der Kolk, and A. Bilandzic, *Lect. Notes Phys.* **785**, 139 (2010).

[49] P. Huovinen and P. V. Ruuskanen, *Ann. Rev. Nucl. Part. Sci.* **56**, 163 (2006).

- [50] H. Niemi, G. S. Denicol, P. Huovinen, E. Molnar, and D. H. Rischke, Phys. Rev. Lett. **106**, 212302 (2011).
- [51] N. Demir and S. A. Bass, Phys. Rev. Lett. **102**, 172302 (2009).
- [52] A. Daher, L. Tinti, A. Jaiswal, and R. Ryblewski, Phys. Rev. D **111**, 074011 (2025).
- [53] F. Capellino, A. Beraudo, A. Dubla, S. Floerchinger, S. Masciocchi, J. Pawłowski, and I. Selyuzhenkov, Phys. Rev. D **106**, 034021 (2022).
- [54] J. D. Bjorken, Phys. Rev. D **27**, 140 (1983).
- [55] S. S. Gubser, Phys. Rev. C **87**, 014909 (2013).
- [56] A. Bagchi, K. S. Kolekar, and A. Shukla, Phys. Rev. Lett. **130**, 241601 (2023,).
- [57] L. Ciambelli, C. Marteau, A. C. Petkou, and P. M. Petropoulos, Class. Quant. Grav. **35**, 165001 (2018).
- [58] A. C. Petkou, P. M. Petropoulos, D. R. Betancour, and K. Siampos, JHEP **09**, 162.
- [59] S. A. *et al.* (ALICE), Phys. Lett. B **790**, 35 (2019).
- [60] S. Weinberg, *Gravitation and Cosmology: Principles and Applications of the General Theory of Relativity* (John Wiley and Sons, New York, 1972).
- [61] D. Dutta, A. K. Mohanty, K. Kumar, and R. K. Choudhury, Phys. Rev. C **61**, 034902 (2000).
- [62] S. Prasad, N. Mallick, D. Behera, R. Sahoo, and S. Tripathy, Sci. Rep. **12**, 3917 (2022).